Université Claude Bernard Lyon I, Institut de Physique Nucléaire
DEA Particules, Noyaux, Atomes et Photons

Contribution à l'amélioration de la calibration de l'électronique auprès de l'expérience DØ au Tevatron

Stéphanie BEAUCERON

Stage effectué au LPNHE - Paris 6 & 7

18 février - 29 juin 2001

Responsable : M. Gregorio BERNARDI

Remerciements

Je remercie Jean-Eudes Augustin, directeur du Laboratoire de Physique Nucléaire et de Hautes Energies des Universités Paris 6 et 7, pour m'avoir permis d'effectuer ce stage dans son laboratoire et pour tous les moyens aussi bien humains que matériels qu'il a mis à ma disposition.

Je tiens à remercier Gregorio Bernardi de m'avoir accueilli au sein de son groupe. Ses conseils tout au long du stage m'ont permis de visualiser la complexité de l'électronique de lecture d'un détecteur.

Un autre aspect de la recherche est le travail en groupe. J'ai ainsi pu bénéficier de l'aide et de l'expérience des différents membres du groupe DØ du LPNHE-Paris. Je remercie donc chaleureusement Ursula Bassler pour sa gentillesse, Bob Olivier pour sa très grande disponibilité, Tibor Kurca pour son soutien ainsi qu'Evelyne Lebreton qui a mis en place et m'a appris l'utilisation du matériel informatique nécessaire.

Je voudrais aussi remercier les physiciens de la collaboration DØ à Fermilab qui gèrent les multiples problèmes rencontrés lors de l'utilisation des logiciels de l'expérience DØ.

Un grand merci également aux thésards du laboratoire pour le délicieux accueil qu'ils m'ont fait (surtout quand il n'y a pas de cannelle dans les gâteaux...).

Contents

Introduction

DØ is one of the detector of the Tevatron collider (Fermilab near Chicago, USA). The collider ring of a diameter of 2 kilometers, allows to have an energy of 2 TeV in the center of mass of the proton-antiproton collisions. The current upgrade of the accelerator and the detector will permit to carry on the search of new particles and in particular the Higgs bosons and the hypothetical supersymmetric particles. The main upgrade of the Tevatron is a new main injector and an improvement in the acceleration process which brings an increase of the instantaneous luminosity by a factor of twenty and an increase of the energy by 10%. Concerning the DØ detector, the main upgrade is an improvement of the tracking system and the addition of a magnetic field, which will allow to measure precisely the momentum of charged particles.

The detector is currently in a commissioning period in order to debug all its different parts. It has already taken data but futher tests are still necessary to obtain a fully functional, reliable and calibrated apparatus. At the LPNHE we are contributing to the debugging of the calorimeter's electronics, which makes intensive use of the online calibration system built at the laboratory in collaboration with LAL Orsay.

My training period was devoted to a first overview on the Higgs search at the Tevatron, and, for the main part, to study the electronics response of the calorimeter to the online calibration system. The aim of these studies were to find dead channels in the electronics and possible problems in the different components of the electronics chain. Moreover we have to determine the parameters which have to be used in the different levels of the electronics and calibration system. These parameters are the delay value to obtain the maximal response of the read out electronics to a calibration pulse and calibration coefficients for the intercalibration of the gains and the response of the 55000 channels.

The first point of this report contains an explanation of the Higgs search startegy at DØ followed by a brief description of the detector. More emphasis is put on a description of the calorimeter electronics and the introduction of the online calibration system before giving a discussion of the results obtained when varying the delay and the amplitude values of the calibration pulse.

Chapter 1

Higgs Search at DØ

One of the main current goals of high energy physics is the discovery of the Higgs boson(s) [1]. Its existence is related to the generation of elementary particle masses. A problem in designing suitable experiments is that the Higgs boson mass is not predicted by the theory. However, its coupling to other particles are predicted.

1.1 Higgs Models

1.1.1 Standard Model Higgs

The Standard Model (SM) [2] appears close to final experimental verification. In the SM, the electroweak symmetry is broken. Indeed, the mass of the $W^{\pm}$ and Z^0 bosons should be zero if the symmetry was conserved. One solution to generate their masses is to add a Higgs doublet (ϕ) containing two complex scalar fields with a non symmetric minimal energy. The lagrangian containing this doublet is given in Eq. 1.1:

$$L_{Higgs}(\phi) = \partial_\mu \phi^\dagger \partial^\mu \phi - \mu^2 \phi^\dagger \phi + \lambda(\phi^\dagger \phi)^2 \tag{1.1}$$

The energy minimum is $\phi_0 = \sqrt{-\mu^2/(2\lambda)}$.

Bosons and fermions get a mass by interacting with these fields. Associated with these scalar fields is the existence of a massive scalar particle, the Higgs boson. The mass of this particle is linked to the vacuum expected value ($v = 246$ GeV) by : $m_h^2 = \lambda v^2$ where λ, the Higgs Yukawa coupling parameter, is not determined by the theory.

As the SM does not incorporate the gravity, it cannot be a fundamental theory. Many extensions of the SM have been studied and the main one is the Supersymmetry theory (SUSY).

1.1.2 Minimal Supersymmetric Extension of the Standard Model Higgs

SUSY is a spin symmetry in which each SM fermion (boson) has a boson (fermion) as SUSY partner. In SUSY, there are many unknown parameters. In order to begin our study of Higgs bosons in low energy Supersymmetry [3], the simplest realistic model of low energy Supersymmetry is taken: the Minimal Supersymmetric extension of the Standard Model (MSSM). In SUSY there is not an unique Higgs doublet as in the SM, but two Higgs doublets. One of these two Higgs field doublets, with a vacuum expected value (vev) v_1, couples to the down quark family and the charged leptons while the second, with vev v_2, couples to the up quark family only. Considering CP invariance, Higgs bosons are grouped into two CP even neutral scalar Higgs bosons, one CP odd neutral scalar and two charged Higgs bosons. Only two parameters are needed to fix all Higgs bosons masses and couplings: $\tan\beta = v_2/v_1$ and the CP odd scalar Higgs mass. In the MSSM, the mass of the lightest Higgs boson is predicted to be less than ~ 135 GeV. The MSSM Higgs search will require a higher integrated luminosity than the search of SM Higgs because in the MSSM, the Higgs production cross section is related to the SM Higgs cross section by a factor lower than 1.

For this reason the search for the Higgs boson will be initially done in the SM framework at the Tevatron.

1.2 Higgs Searches

The inclusive Higgs cross section is of the order of 1 pb with a Higgs mass of 120 GeV. The most relevant decay branching ratio of the SM Higgs boson are given in Fig. 1.1.

For Higgs masses lower than 135 GeV, the decay into fermion anti-fermion dominates with a dominant branching ratio for $h_{SM} \to b\bar{b}$. For larger masses, the W^+W^- and Z^0Z^0 are the dominant decay channels.

At the Tevatron the two main SM Higgs production processes are $q\overline{q} \to V^* \to Vh_{SM}$ [$V = W^\pm$ or Z^0] and $gg \to h_{SM}$. For the second process, the signature $h_{SM} \to b\bar{b}$ is not promising at the Tevatron due to an overwhelming QCD background of $b\bar{b}$ production. In order to discover a Higgs signal, the signal must be separated from the SM backgrounds.

For a low SM Higgs mass (90 GeV $\leq m_h \leq$ 130 GeV) the $q\overline{q} \to V^* \to Vh_{SM}$ mode dominates and different final states exist as a function of the V decay. V boson can decay into lepton and neutrino, into two neutrinos or into two leptons or two quarks. In Tab. 1.1 are given the combined results and the corresponding SM background of CDF (CDF is the second detector of the Tevatron) and DØ experiments for these different finals states. In this table, results are given for three differents analysis : SHW with sequential cuts (SHW is a simple simulation of the "average" CDF and DØ detector response), SHW with neural network analysis and an improvement of the CDF Run I analysis. The dominant channel $\ell\nu b\bar{b}$ has the highest signal over square root of background ratio ($S/\sqrt{B}$) for masses between 110 and 120 GeV for all 3 analysis. Moreover the neural network analysis reduces the background by an additional factor of two.

Table 1.1: Summary of low mass Standard Model Higgs search channel sensitivities used in the combined integrated luminosity threshold calculations. The values of signal(S) and background(B) are expressed as the number of events expected per detector in 1 fb^{-1}. Here we assume an improved Run II m_{bb} resolution of 10%. "SHW" indicates the analysis based on the SHW simulation, "NN" indicates the SHW neural network based analysis, and "CDF" indicates the analysis based on extrapolations from the CDF Run I conditions to Run II detector geometry and efficiencies.

		Higgs Mass (GeV)				
Channel	Rate	90	100	110	120	130
	S	8.4	6.6	5.0	3.7	2.2
$\ell\nu b\bar{b}$ (CDF)	B	48	52	48	49	42
	$S/\sqrt{B}$	1.2	0.9	0.7	0.5	0.3
	S	10	8	5	4	3
$\ell\nu b\bar{b}$ (SHW)	B	75	68	57	58	52
	$S/\sqrt{B}$	1.1	1.0	0.7	0.5	0.4
	S	8.7	9.0	4.8	4.4	3.7
$\ell\nu b\bar{b}$ (NN)	B	28	39	19	26	46
	$S/\sqrt{B}$	1.6	1.4	1.1	0.9	0.5
	S	2.5	2.2	1.9	1.2	0.6
$\bar{\nu}\nu b\bar{b}$ (CDF)	B	20.0	18.6	16.0	13.0	9.6
	$S/\sqrt{B}$	0.6	0.5	0.5	0.3	0.2
	S	8.9	6.7	4.6	3.2	2.1
$\bar{\nu}\nu b\bar{b}$ (SHW)	B	77	69	56	39	30
	$S/\sqrt{B}$	1.0	0.8	0.6	0.5	0.4
	S	12	8	6.3	4.7	3.9
$\bar{\nu}\nu b\bar{b}$ (NN)	B	123	70	55	45	47
	$S/\sqrt{B}$	1.1	1.0	0.8	0.7	0.6
	S	1.0	0.9	0.8	0.5	0.3
$l^+l^-b\bar{b}$ (CDF)	B	3.6	3.1	2.5	1.8	1.1
	$S/\sqrt{B}$	0.5	0.5	0.5	0.4	0.3
	S	1.5	1.2	0.9	0.6	0.4
$l^+l^-b\bar{b}$ (SHW)	B	4.9	4.3	3.2	2.3	1.9
	$S/\sqrt{B}$	0.7	0.6	0.5	0.4	0.3
	S	1.2	0.9	0.8	0.8	0.6
$l^+l^-b\bar{b}$ (NN)	B	2.9	1.9	2.3	2.8	1.9
	$S/\sqrt{B}$	0.7	0.7	0.5	0.5	0.4
	S	8.1	5.6	3.5	2.5	1.3
$q\bar{q}b\bar{b}$ (SHW)	B	6800	3600	2800	2300	2000
	$S/\sqrt{B}$	0.10	0.09	0.07	0.05	0.03

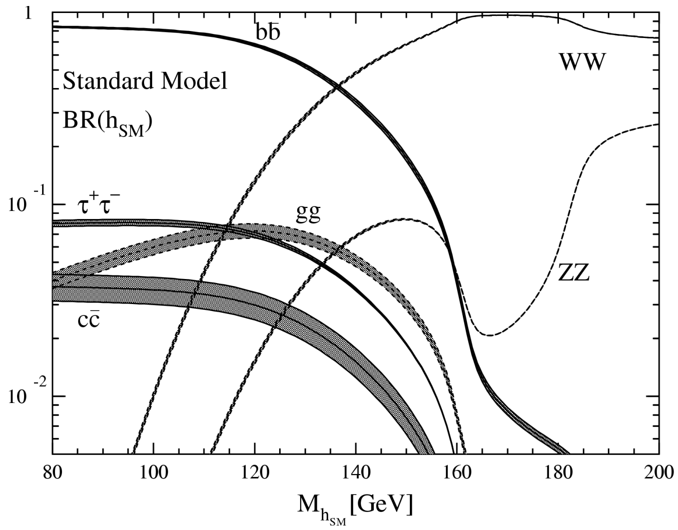

Figure 1.1: *Branching ratio as a function of the Standard Model Higgs mass. The $b\bar{b}$ decay channel is dominant for SM Higgs mass lower than 130 GeV.*

1.3 $Wh_{SM} \to l\nu b\bar{b}$ Decay Channel

For this channel which is the dominant one at low Higgs mass, the background comes from these SM processes: $Wb\bar{b}$, WZ, $t\bar{t}$, t; they have the same signature as the signal. The events are selected if they have a lepton transverse momentum $p_T(l) > 15$ GeV with a pseudorapidity $|\eta_l| < 2.0$, two jets with a transverse energy by jet $E_T^{jet} > 10$ GeV with a pseudorapidity $|\eta_{jet}| < 2.0$ and a missing transverse energy $\not{E}_T > 20$ GeV.

To trigger on the b quark jets the secondary vertex information is used. Indeed, as the b quark decay after a few millimeters, only the tracks with a high impact parameter d_0 are considered. A selection on tracks with high d_0/σ_{d_0} is made in Run II (σ_{d_0} is the error on the d_0 parameter measurement). The trigger efficiency for $Zh_{SM} \to \nu\bar{\nu}b\bar{b}$ events is predicted to be ~80% and ~20% for $Z \to b\bar{b}$ events.

The current studies on the b tagging give an efficiency of 40% per jet with less than 1% of fake identification coming from the lighter u, d, c and s quarks.

1.4 Higgs and Calibration

For Higgs masses lower than ~135 GeV the most promising channels at the Tevatron involve the decay of the Higgs into $b\bar{b}$. The signal is seen as an excess of events having a $b\bar{b}$ invariant mass peaked at the Higgs mass over the background. Obtaining the best possible invariant $b\bar{b}$ mass resolution is crucial to extract the signal. Considering an integrated luminosity of 1 fb^{-1} and a Higgs mass of 120 GeV with an invariant $b\bar{b}$ mass resolution of 15%, 4 signal events versus 119 background events are expected. With the same luminosity and Higgs mass but with a $b\bar{b}$ mass resolution of 10%, 4 signal events versus 58 background events are awaited. The mass resolution will be achieved by improving the calorimeter calibration.

1.5 Conclusions

One of the last results of LEP is an evidence for a SM Higgs boson with a mass of 115 GeV, at the ~3 sigma level (combined results from LEP experiments november 2000 [4]). In Fig. 1.2 is described the Higgs mass reach as a function of the integrated luminosity at the Tevatron. In the first period of data taking (Run IIa) and after 2 years of running a 115 GeV Higgs mass could be either confirmed or excluded at 95% confidence level. To obtain a 3 σ level at this mass, a luminosity of 5 fb^{-1} is required and can be reached in the year 2004-2005. A 5 σ discovery requires 15 fb^{-1} (2007) of combined result between DØ and CDF. With the same luminosity the exclusion at 95% confidence level will be extended to exclude the SM Higgs up to 185 GeV, if it does not exist in that mass range.

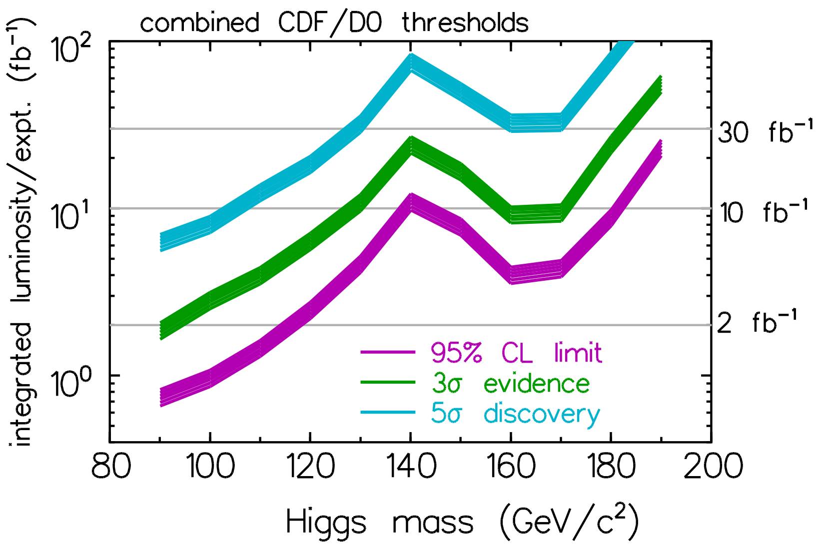

Figure 1.2: *Higgs mass reach as a function of the Tevatron integrated luminosity and for different sensitivity levels (2σ, 3σ, 5σ). For a Higgs mass of 115 GeV, less than 2 fb^{-1} are required to exclude it at 95% confidence level.*

Chapter 2

The Experimental Apparatus

The Tevatron is a proton-antiproton collider located at Fermilab, near Chicago. The accelerator provides beam collisions in two points, equiped with the CDF and DØ detectors. A third interaction region is actually prepared for the BTeV experiment.

2.1 The Tevatron

The first running period of the Tevatron started in 1989 and last until 1996. During this time both experiments accumulate approximately 120 pb^{-1} of integrated luminosity. Since then, the Tevatron was shutdowned in order to upgrade the accelerating system. The main improvement is the replacement of the Main Ring Injector which was located during Run I in the Tevatron tunnel by the Main Injector in a new tunnel and the addition of a recycling facility for the antiprotons.

The protons are produced by accelerated H^- ions which loose their electrons by passing through a carbon sheet. The protons producted are introduced in the Main Injector where they are grouped into 5 to 7 bunches of 6 10^{10} protons. The antiprotons are generated by proton collisions on a copper and nickel target. The antiprotons are brought to the Main Injector where 1.3 10^{10} antiprotons are accumulated in 8 hours. At the end of each Tevatron store, beams are decelerated and the antiprotons are extracted into the antiproton recycler, and re-used for a subsequent store.

The upgrade of the Tevatron is expected to increase the instantaneous luminosity up to 2 $10^{32}\mathrm{cm}^{-2}\mathrm{s}^{-1}$ with a time bunch crossing of 396 ns. The energy in the center of mass increases from 1.8 TeV to 2 TeV. These new running conditions of the Tevatron required an upgrade of the two detectors.

2.2 The DØ Detector

During a proton-antiproton collision at high energy, many particles are produced. The DØ detector [5] is designed to study processes with high transverse momentum. To detect all different particles, the detector is composed by several sub-detectors as described in Fig. 2.1. From the interaction point to the outside of the detector are successively placed the tracking system, the calorimeter and the muon chambers.

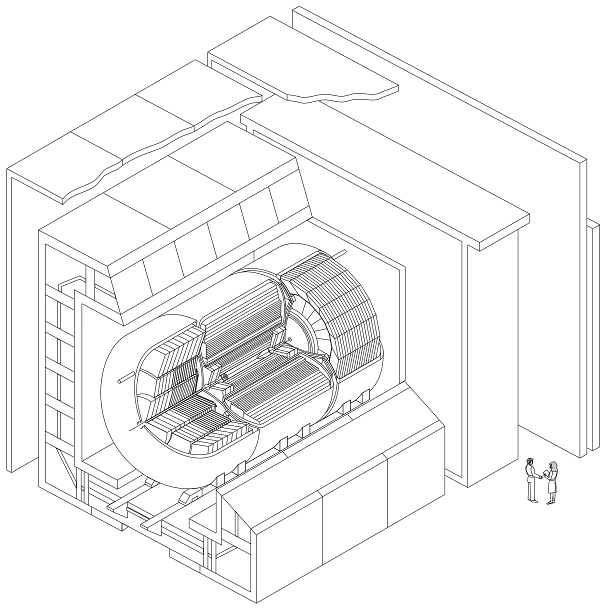

Figure 2.1: *View of the DØ detector. The cylindrical part corresponds to the calorimeter. The muons chambers surrond the calorimeter.*

2.2.1 Tracker and Preshower

The tracking system is constituted by a silicon vertex [6] detector and a scintillating fiber tracker. The silicon tracker is the main resolution part of the tracking system and is the first set of detectors encountered by particles emerging from the interaction point. The tracker system measures the tridimensional trajectory and the curvature of tracks in a magnetic field of 2 Tesla. From the curvature value, the momentum of charged particle can be determined. Moreover, by combining the information of all the tracks, the interaction point (vertex) can be reconstructed. The high resolution of the silicon detector allows to even reconstruct secondary vertices from particle decays and plays a major role in the b quark tagging. All the signals going through these detectors are read out by an advanced electronics system.

Between the tracking system and the calorimeter, the preshower detector is designed to aid electron identification and to correct energy losses in the solenoid. The preshower acts as a calorimeter owing to an energy sampling, and as a tracker with its precise position measurement.

2.2.2 Calorimeter

The calorimeter surrounding the tracker and the preshower, uses Uranium as absorber and liquid Argon as active media. In the absorber the interaction of particles with dense matter slows the particles down producing showers of secondary particles which are ionising the active media proportionnaly to the initial energy. Liquid Argon has the advantage to be mostly insensitive to radiation and shows a very stable behaviour in time, compared to other active materials as for example scintillator. Uranium is the densest possible material and allows therefore to build a very compact apparatus.

The calorimeter is made by sandwiches of layers of absorber (Uranium), readout electronics cards and an active medium (liquid Argon). The calorimeter is longitudinaly sampled by layers crossed by the particles and is transversaly divided in cells as a function of the pseudo-rapidity η and the azimutal angle φ which allows to localize the particles in the detector. All cells in a same longitudinal layer are called in the same depth and all cells in the same $\eta \times \varphi$ are in the same tower. The calorimeter respects a pseudo-projective geometry described in Fig 2.2. Each calorimeter cell consists of a 2.3 mm liquid Argon gap between

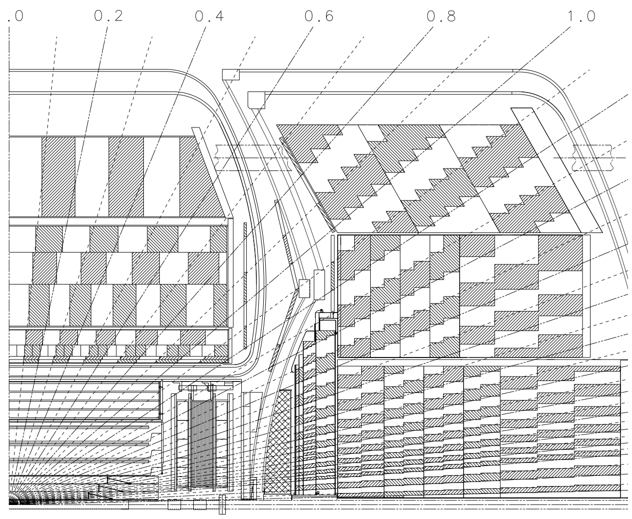

Figure 2.2: *Pseudo-projective geometry of the DØ calorimeter.*

an absorber plate and a readout board (cf. Fig. 2.3).

The readout board has a high resistivity coating, to which a potential is applied with respect to the absorber plate in order to create an electric field. After a charged particle ionizes the active medium, the electrons from the ionisation drift under the influence of the electric field to the readout board which measures the created current. This current is proportionnal to the energy lost by the particle in the medium.

The calorimeter is separated in two parts: the electromagnetic calorimeter and the hadronic calorimeter. The electromagnetic calorimeter allows to measure showers produced

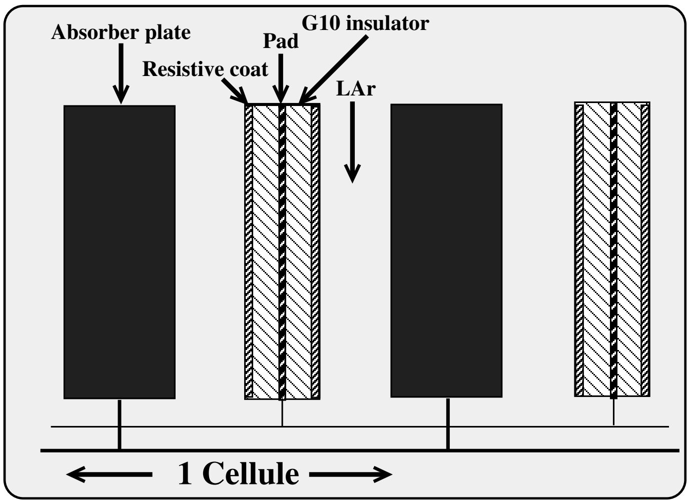

Figure 2.3: *A calorimeter cell constitued by 2 absorber plates surrounding the readout board. The active medium used is liquid Argon.*

from the interaction of the electrons and photons, whereas the longer and wider showers produced by hadrons are only contained in the hadronic section of the calorimeter, surrounding the electromagnetic part. In the hadronic section, the absorber medium is made of steal and the cell size and the capacitance are larger. Moreover, the calorimeter is divided in separated cryostats: the central (CC), and two endcap calorimeters (north and south). Besides the readout board which collects the drifted electrons in a calorimeter cell, the calorimeter electronics amplifies, shapes and buffers the signal until a trigger decision has been taken.

The arrangement of the different modules in the calorimeter and the cryostat is done in order to reduce dead materials and obtain a quasi hermetic detector. The electronics of the calorimeter is going to be discussed in the following section.

The energy resolution of the electromagnetic calorimeter depends on the calibration of the electronics. Indeed, the electromagnetic resolution can be parametrized as:

$$\Delta E/E = C \oplus S/\sqrt{E} \oplus N/E \tag{2.1}$$

where C is a constant term depending on the electronics calibration, S is the sampling term and N is the noise term. The aim is to calibrate the electronics better than 1%.

2.2.3 Muon Chamber

The last detector layer is dedicated to the detection of muon: indeed, after the calorimeter the only particles which have not been absorbed are muons and neutrinos. The muon chambers [7] are made of Proportionnal Drift Tubes (PDT) surrounding a toroidal magnet which produces a magnetic field, curving the muon trajectories and allowing therefore to measure their momenta.

The neutrinos which interact only by weak interaction are the only undetected particles, so they can be identified by the transverse energy imbalance obtained from the complete event. The main contribution to this measurement is due to the calorimeter.

2.3 Triggering and Data Acquisition

The total inclusive cross section of $p\bar{p} \to X$ events is around 70 mb at $\sqrt{s} = 1.8$ TeV. With a luminosity of $2 \times 10^{32}\mathrm{cm}^{-2}\mathrm{s}^{-1}$, the event rate is 14 MHz. The current technology is not able to record all these events. Moreover, only inelastic collisions are interesting, therefore events have to be selected.

Due to this high collisions frequency, the decision to record or not an event must be taken quickly. As a full analysis before recording cannot be performed, three successive levels of fast decision are created and the precise studies of the event are only made at the last level.

The first level (L0) indicates only if the event is the result of an inelastic collision. If the event pass the L0 level, the L1 level examines which types of particles have been seen by the different parts of the detector (by addition of measured energy in the calorimeter and tracks in the muon chamber). At the L2 level, electromagnetic and hadronic candidates are searched. The L3 level gives the first characteristics of the particles in the event. The final rate event recording is about 10 Hz.

Chapter 3

The Calibration System of the Calorimeter Electronics

One of the salient components of the DØ detector is its hermetic, highly stable, radiation hard liquid Argon calorimeter discussed in Chapter 2. The calorimeter upgrade concerns only its electronics and has been designed to operate reliably and with small deadtimes for an instantaneous luminosity of $2 \times 10^{32}\mathrm{cm}^{-2}\mathrm{s}^{-1}$ and a bunch crossing time of 132 ns. The two requirements of the upgrade are a reduction in shaping and readout time, and analog buffering needed to store data until the level-1 or level-2 trigger decisions are available. These tasks needs to be performed while maintaining the properties of low electronics noise, high linearity and good accuracy, i.e. small variations in channel-to-channel response. Test-beam data have shown that the energy resolution of the electromagnetic calorimeter due to stochastic fluctuations of the electromagnetic showers can be parameterized as $S/\sqrt{E}$, where S is measured to be around 15% in the CC. The unit gain of the liquid Argon calorimeter helps to keep the response stable over time. In order to fully exploit these qualities of the calorimeter and achieve good energy scale accuracy and resolution, it is essential that the calorimeter readout electronics [8] is highly linear, stable and produces very little electronics noise.

There are two steps in the energy calibration. The first one is the online calibration which is a study of a response to a very well known injected calibration signal ("pulse"). The second one is the offline calibration which is obtained with physics events characterized by a known energy (for example the Z^0 mass peak). In this report we will study only the online calibration.

3.1 Calorimeter Electronics

The electronics receives a signal from a calorimeter cell which is proportional to the energy lost by a particle going through the active media. Coaxial cables carry the signal to a feed through port which allows to pass them across the cryostat. The feed through boards reorganize signal from the module builder's scheme to the physics scheme in which signals from all depths in an $\eta\varphi$ space are combined to quasi projective 0.1×0.1 towers delivered on two 24 channel cables. The signal is then conducted to the preamplifiers. The preamplifiers are small hybrid ceramic printed circuits, which are themselves mounted on a printed circuit motherboard. The charge sensitive preamplifiers integrate the image charge produced by the calorimeter cells to produce proportional voltages. The preamplifier outputs go through 30 meters of cable to a BLS (baseline subtractor) system which shapes the signal and samples it before and after the bunch crossing.

The aim of the BLS is to subtract the signal baseline before an interaction from a signal just after it in order to get the exact signal amplitude. The sampled signal is stored in a buffer which consists of an array of capacitors called Switched Capacitor Array (SCA). The SCA resolution allows for a 12 bits dynamic range. In order to obtain a 15 bits range two shaped outputs are provided with $\times 1$ gain and $\times 8$ gain by the preamplifier. Following the level-1 trigger decision the readout with the appropriate gain factor is digitized by an Analog Digital Converter (ADC).

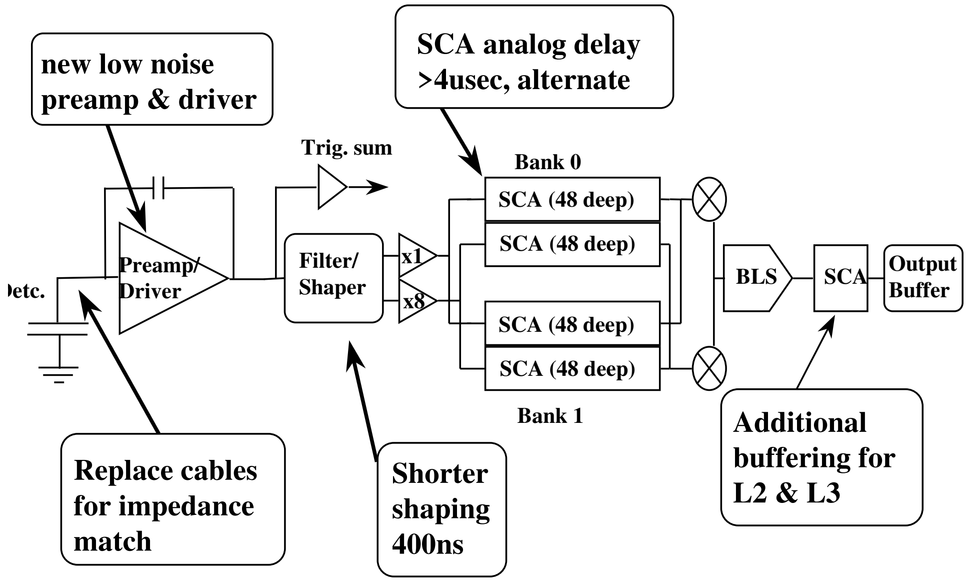

Figure 3.1: *Schematic view of the electronics system for the DØ calorimeter at Run II. The added text corresponds to the modification performed after Run I.*

In Fig. 3.1 is shown a schematic view of the electronics with the changes made for Run II in order to reduce electronics noise and deadtime. The readout electronics of the DØ calorimeter is composed by 12 crates containing 12 ADC cards. Each card contains 384 channels which are distributed on 8 BLS cards, each treating the signals of 4 Towers of 12 longitudinal depths. In order to calibrate the detector, the response of the different elements needs to be well known. The response before calibration is expected to differ from channel to channel at the level of a few percents.

As the calorimeter is made in two parts (electromagnetic and hadronic), the electronics cards are divided in two parts as well and each tower contains 7 electromagnetic and 4 or 5 hadronic channels. From the center of the calorimeter, the first channels connected (depths 0-6) are the electromagnetic ones followed by the hadronic channels (depths 7 to 10 or 11). To remain related with the physical sampling of the detector we use the notation of depth, BLS and Tower. The organisation in depth, tower, BLS and connections between the pulser and the preamplifier card are shown in Fig. 3.2. The channel number is related to the BLS, tower and depth positions by:

$$Channel = BLS \times 48 + Tower \times 12 + Depth \tag{3.1}$$

BLS varies from 0 to 7, Tower from 0 to 3 and Depth from 0 to 11.

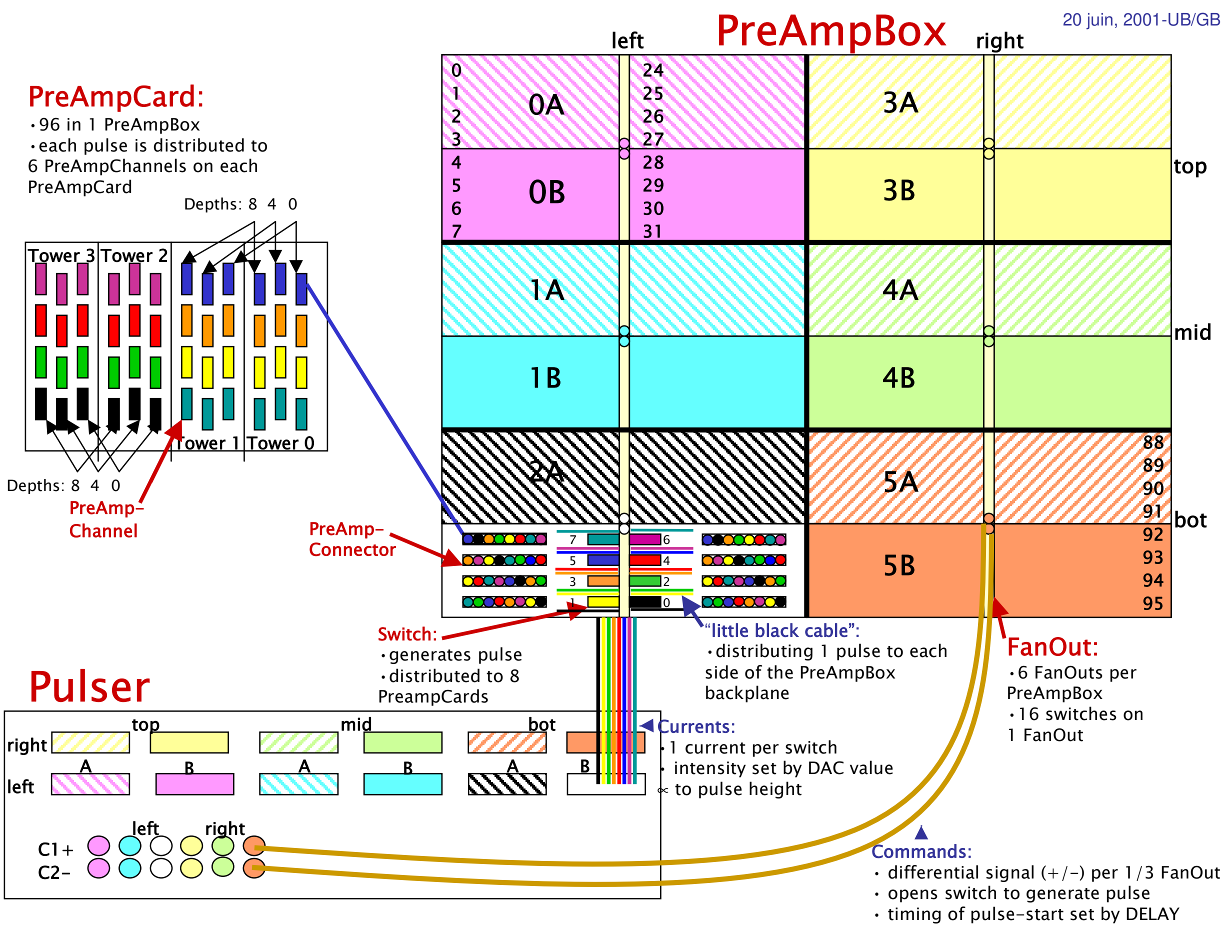

Figure 3.2: *Sketch of a preamplifier box with its connections to the calibration pulsers.*

3.2 Calibration System

The ability to calibrate the DØ calorimeter electronics is of prime importance to determine with an optimal precision the energy of a particle, since a non uniform response degrades both the scale and the resolution of the measurement in particular the constant term (cf. Eq. 2.1).

For an online calibration, a signal given by a pulser is introduced in the electronics chain. This can be done in two ways: either the signal is introduced inside the calorimeter on the reading cell (cold calibration), or it can be generated outside the cryostat just at the beginning of the electronics chain (warm calibration). The first method has the advantage of creating the calibration signal at the same place as a true particle but this method needs an access to the inside of the cryostat which was not foreseen when the detector was built and excludes any repairing in case of problem. Due to the problem of accessibility, the warm calibration has been chosen at DØ.

The calibration system of the DØ calorimeter consists of 12 identical subsystems. Each subsystem is composed of one Pulser Mother Board which sends the signal distribution, the commands and the DC currents to two cards called active fanouts. They are called active because in addition to perform the signal distribution, the switches generate the calibration pulse.

The Pulser Mother Boards are connected via a serial bus interface to an input-output VME card, the Pulser Interface Board (PIB) with which the controls of the amplitude and the signal calibration delay are done together with a selection of pulsed channels. The Pulser Mother Board are composed of one serial bus interface, one channel enable register, one Digital Analogic Converter of 18 bits, six programmable delays and 96 DC current generators programmable by the DAC.

On the reception of a trigger signal, three commands are sent to each of the two corresponding fanouts. The pulse generated by the actives fanouts cards are near the preamplifiers. The shortness of the cable linking the active fanout to the preamplifier prevents losses and perturbations of the pulse. The conversion of the current to the calibration signal is performed on the “switch” cards which consists of an Operational Amplifier with a little shift register, a transistor and a resistor.

The active fanout is divided into three identical parts. Each part receives one command signal and 16 DC currents, a different delay can be set for each command. The command signal switches the DC current from ground to a load, which shapes the calibration signal. The produced calibration signal is an exponential signal with a short rising time (60 ns) and an exponential decreasing signal with a decreasing time of 400 ns. Each calibration signal is sent via the short cables to 4 preamplifier boards, hitting 6 preamplifiers on each board. So one pulser is connected to 48 preamplifiers.

The calibration system has been designed and built by the LPNHE and Orsay laboratories from fall 1998 to fall 2000. It has been installed at DØ in october 2000 [9].

3.3 Parameters Definition

The studies performed in this report are devoted to the response to a calibration signal through all the electronics chain.

The two main parameters studied here are the delay of the pulsed signal and its amplitude. For the calibration, the time between the pulse sent and the sampling for a physics event must be optimized to get the maximal signal. The time interval is fixed for physics events, but can be varied in the case of a calibration run where a delay on the pulse start can be introduced. This is necessary, as the pulser shape is different from the shape of the signal in a physics event. Simulation studies have shown that the best calibration is obtained when the calibration signal is read out at its maximum. The delay time variations are sketched, in Fig. 3.3. The delay can be moved by steps of 1.67 ns, which is the definition of one delay unit, owing to delay line in the Pulser Mother Boards. A scan over a large range of delay values, allows to reconstruct the pulse shape.

The absolute amplitude is a parameter which is related to the energy seen in the calorimeter. The response of the electronics chain to a given pulse height has to be the same for all channels and each gain path for all amplitudes. The behaviour of the electronics should also be linear i.e. for a variation in the pulse amplitude a proportionnal variation in the readout should be seen.

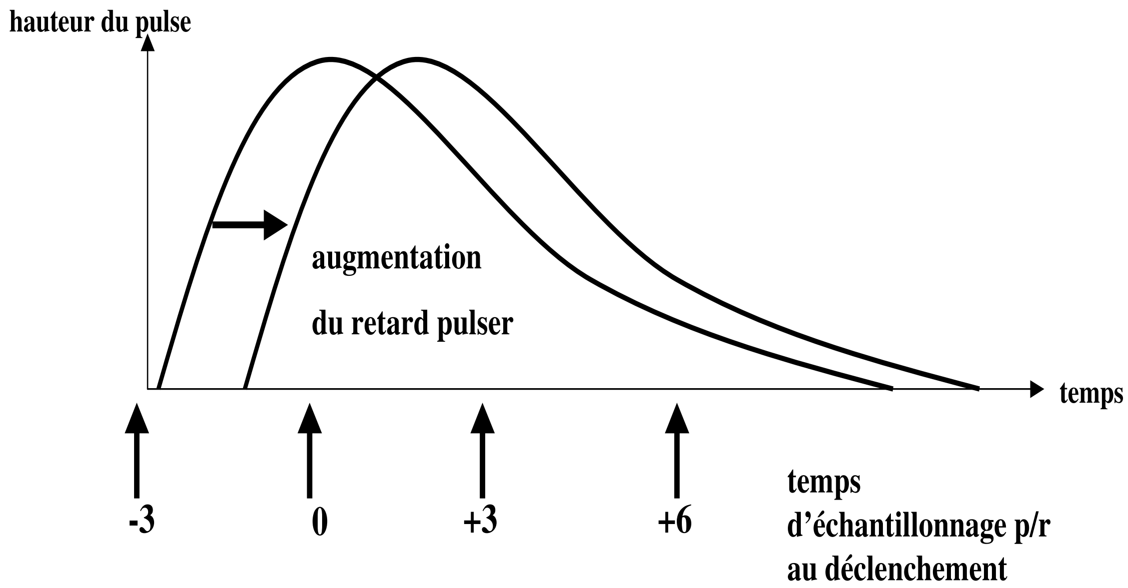

Figure 3.3: *Schematic view of the influence of the calibration delay with respect to the sampling time. This calibration must be adjusted in order to shape the signal at its maximum of amplitude. Any timing miscalibration induces a degradation of the signal resolution.*

Chapter 4

Calibration Measurements and Results

The Cal_elec "online" program [10] allows to study the response of the 55,000 calorimeter channels, providing for instance the mean and sigma values of the response of the channels. The first studies have only been done using the central calorimeter crates (numbered 2,3,8,9) which contains a large fraction of the central calorimeter cells but also a small fraction of the endcap calorimeter cells. This layout is due to the fact that the towers are in projective configuration with respect to the interaction point, and so a tower at —η—=1 extends over the central and encap calorimeter.

4.1 Process

On a plot of Cal_elec (cf. Fig. 4.1), the mean value for a ADC card (384 channels) is represented. Fig. 4.1.a describes a typical output distribution. In the test made, not all channels of central calorimeter crates were connected or pulsed and therefore no signal is present on these cells. In the central calorimeter crates, the last depth of each tower is not connected. The unpulsed channels are not the same for all cards so a "correction" function was made to obtain a plot without "holes" (cf. Fig. 4.1.b) which allows an easy finding of dead channels. The pattern of the unpulsed channels is represented in Fig. 4.1.c. To keep the physics informations (i.e. to see if a channel is a bad one, or not in agreement with the other channels), the correction of unpulsed channels is just an addition of the difference between the mean value of pulsed channels and the mean value of unpulsed channels.

Using the pulser, our studies had two aims. First to determine the value of the best delay, i.e. the one which gives the maximum response allowing to determine the value of pedestal and the slope of the signal when the amplitude of the pulse is varied. Only the connected, pulsed channels are considered. Twenty runs have been taken with a delay varying from 0 to 190 by steps of 10 with a value of amplitude equal to 40,000. The second goal was to study the linearity of the electronics chain. Ten runs have been taken with an amplitude going from 10,000 to 100,000 by step of 10,000 with a delay value of 50. In these runs taken

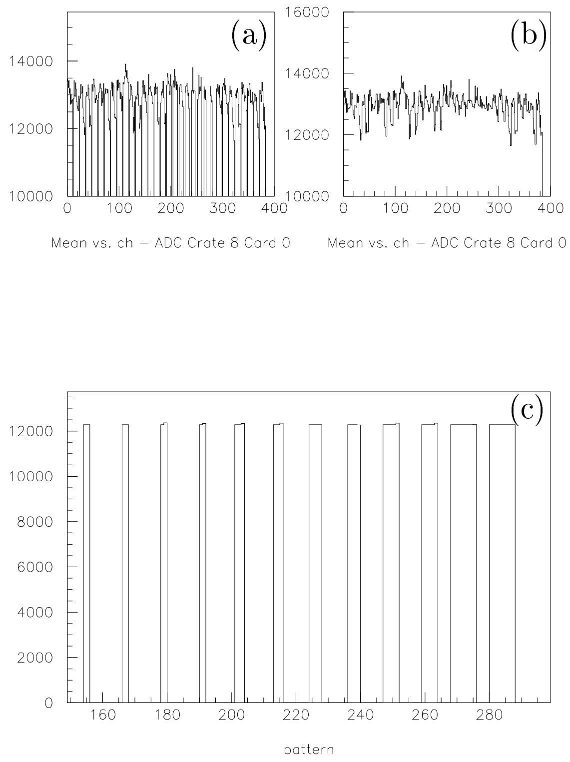

Figure 4.1: *(a) A typical outside plot from Calelec; (b) the same plot corrected as function of unconnected channels (all the 12th) and unpulsed channels; (c) the pattern of unpulsed channels.*

at that time the crate 3 displayed a strange pattern. Some studies on the timing and control of this crate allowed to correct the problem encountered.

4.2 Time Calibration

The result of the twenty runs of delay, are combined to show the mean value as a function of the delay value for a specific channel. In Fig. 4.2 two kinds of channels can be distinguished either connected to an electromagnetic or a hadronic calorimeter cell. The reconstructed pulse shape is very different for the two channel types. This is explained by the fact that the pulse shape depends on the detector capacity which is related to the cell of the calorimeter. Indeed this detector capacity varies by about a factor of ten from electromagnetic channels ($\sim$ 0.4 nF) to hadronics channels ($\sim$ 4 nF). The variation in the pulse shape is due to the reflexion of the signal in cable towards the detetor and this reflexion depends on the capacity. The reflexion is fast for electromagnetic channels and slow for hadronic channels. Electromagnetic channels which correspond to the first 7 depths can be fitted quite well by a second order polynomial function as shown in Fig. 4.2.a . Due to large influence of the reflexions in the hadronic channels, a second peak is created at high delay value which can be fitted with a sixth order polynom (cf. Fig. 4.2.b).

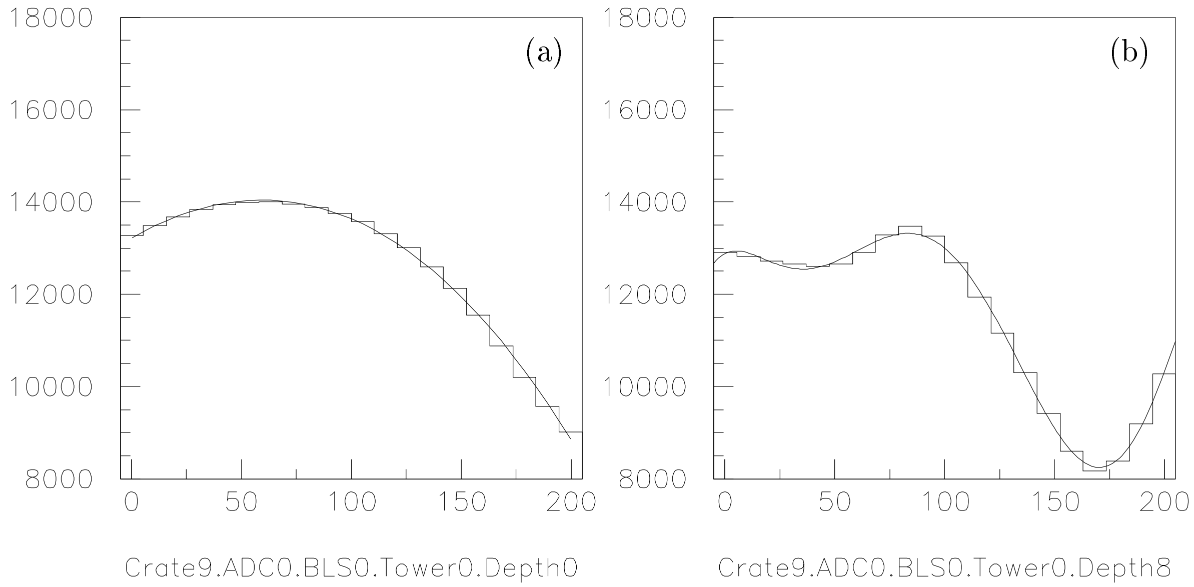

Figure 4.2: *Plots of variation of the mean value as a function of the delay for the same crate, card, BLS, Tower but for different depth: (a) an electromagnetic channel; (b) an hadronic channel.*

After the fit, the fit parameters are studied, first to determine the delay at which the maximum value of the curve is obtained; secondly to control the stability of the fit parameters through all the depths of all the towers. In Fig. 4.3, the plots of the values of the fit parameters have two differents patterns. For electromagnetic channels (cf. Fig. 4.3.a,c), all fit parameters are quite constant as a function of depth and as a function of the card. This allows us to determine an unique delay value.

The hadronic delays are not stable (cf. Fig. 4.3.b,d). This could be due to different values of the capacitance which create the reflexions and their possible variation according to the depth and crate values.

Moreover, when we look at the second fit parameter in Fig. 4.4, we can observe for a specific depth, for all the BLS in a given ADC card a “2 channels” pattern. The explanation of this phenomena comes from the way the pulse is distributed on a BLS. Indeed the same signal arrives to two adjacent towers (T0 and T1) for a given depth and another signal arrives to two other adjacent towers T3 and T4. We use the same notation as in Fig. 3.2. The two lines pattern corresponds to each couple of towers (T0 and T1, T2 and T3) and is not a problem related to the pulser.

As a conclusion, the fit parameters are stable as a function of depth, tower, cards, so the delay value at which we obtain the maximum value of the curve is stable. The calculated maximum value, as seen in Fig. 4.5, is around 75 delay units for the electromagnetic channels but increases for the hadronic ones. For the hadronic channels, we assume that the maximum

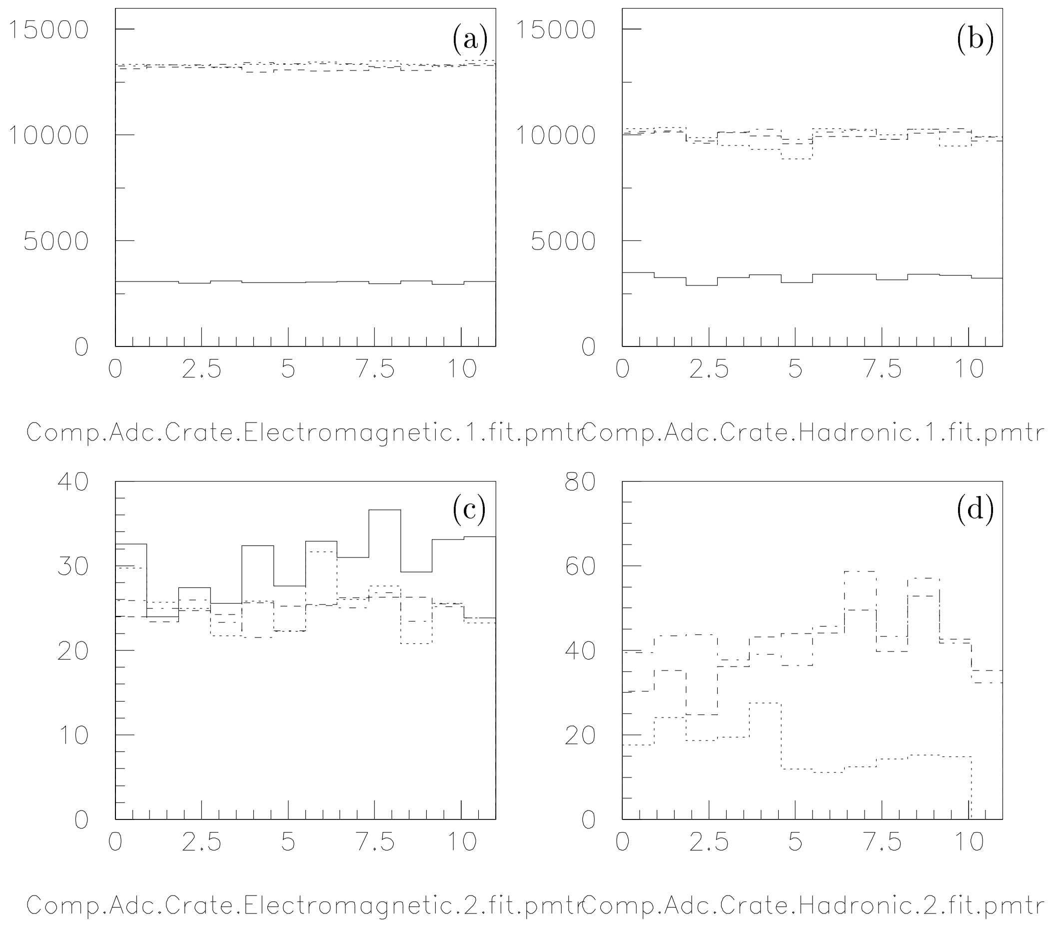

Figure 4.3: *Comparison of the value of the fit parameters as a function of the ADC cards value and for the 4 crates (crate 3 is not in agreement): (a) first fit parameter for an electromagnetic channel; (b) first fit parameter for an hadronic channel; (c) second fit parameter for an electromagnetic channel; (d) second fit parameter for an hadronic channel.*

has to be higher than 60 delay units to avoid the first maximum. When the delay value to obtain the maximum of the curve is superimposed for all cards of a crate as a function of depth (cf. Fig. 4.5), an accumulation is observed. Depths 0 and 1, depths 2 3 4 5, depth 6 and hadronic depths correspond to different groups in the electronics, which are clearly visible in Fig.4.5.

Moreover the value of the maximum depends on the crate. Indeed, if we look at crate 8 and 9 we have a difference of around 15 delay units which is due to a difference in the length of the cables linking each of these crates to the detector.

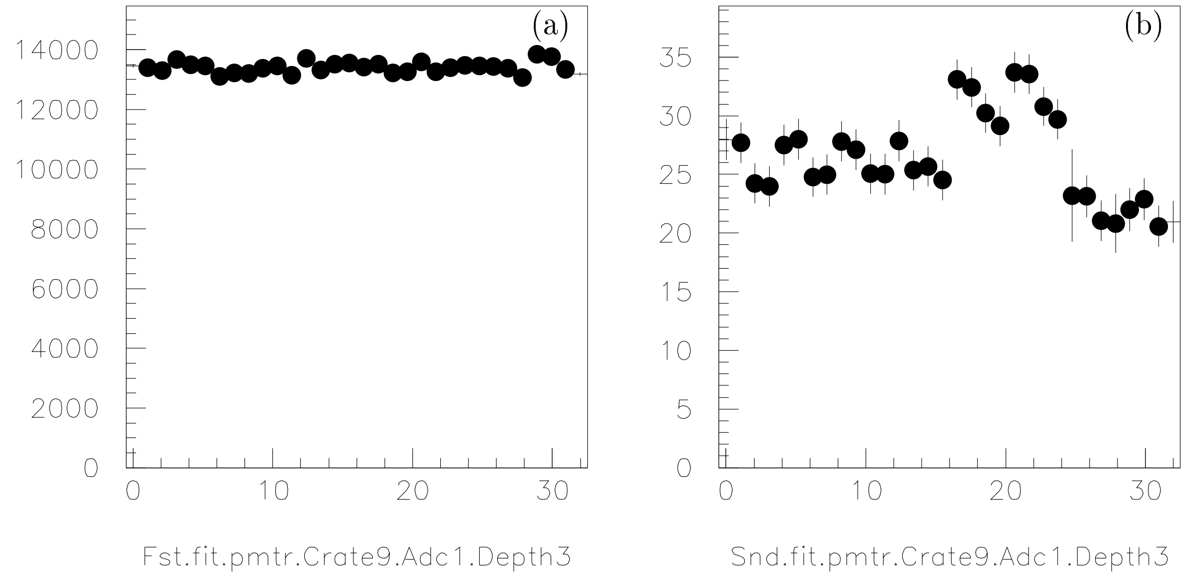

Figure 4.4: *(a) The first fit parameter is a constant value as a function of tower and BLS for the ADC card 1 of crate 9; (b) the second fit parameter in which we observed a 2 by 2 pattern of BLS.*

4.3 Amplitude Calibration

For this study, the mean value of each depth is shown as a function of the amplitude variation for each channel. During the variation of the amplitude, a saturation of the mean value is encountered. This saturation is due to components on the switches. That is why we can not directly study the complete range of the "ramp". We perform a straight line by fitting it in a restricted interval.

To study the slopes of the amplitude ramps, a fit on the first 6 points was found optimal. Indeed for a fit on the first 5 points or for a fit on the first 7 points or for a fit on all points, the value of χ^2 by degree of freedom is significantly higher than for a fit on the first 6 points (cf. Fig. 4.6).

Both electromagnetic and hadronic channels display a good linearity and the error on the slope value is 1.1%.

The pedestal and slope values shown in Fig. 4.7.a,b, are quite stable for the electromagnetic channels but are smaller by about 20% for hadronic channels at large depths since the delay of 50 units was used, and the hadronic response is not at its maximum for this value (cf. Fig 4.2).

Moreover, a comparison of the different crates as a function of cards shown in Fig. 4.8 shows a good agreement in the pedestal and slope values (crate 3 is not in agreement and not considered in this conclusion). However for the card number 8 for one of the crates, we

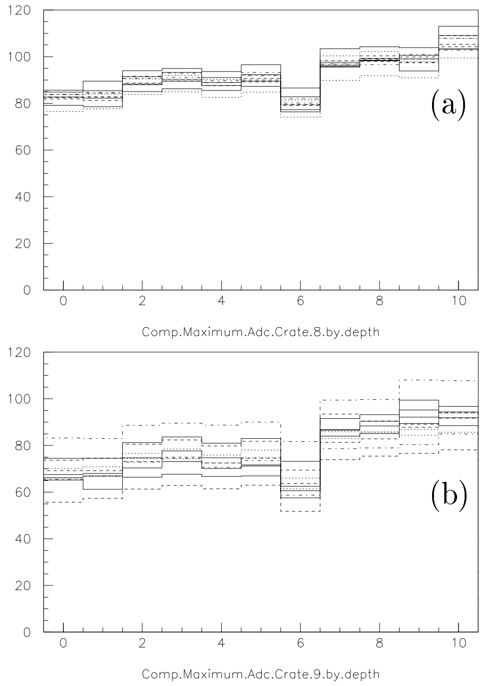

Figure 4.5: *The mean value of the best delay as a function of depth and on which all cards are superimposed : (a) for crate 8; (b) for crate 9.*

have a significantly higher value of the pedestal which is constant for all channels of this card. This card needs to be checked individually with other runs.

As for the delay variation, a 2 by 2 pattern of the BLS is observed on some crates and cards. The previous explanation of this effect remains valid also for the amplitude variation.

As a conclusion, we obtain a quite stable response to amplitude variation for all channels. However the pedestal value is not the same as pedestal measurement without pulsing. The difference is significant: we find a pedestal around 4,200 compared to 4,500 found from pedestal measurements without pulsing, so a difference of around 5 percents. Studies are needed to clarify this point.

4.4 Dispersion Studies

The sigma values are calculated from the distribution of the mean values. The studies of these values tell us if a channel has some problems. Indeed as the mean value is computed for one value of the pulse height, it should be similar for all channels and in the following we are looking at the sigma which has to be low. If we have a high sigma, we conclude that the channel is not stable.

Looking at the plots, in general, the sigma value is varing from 0 to 60 for the delay

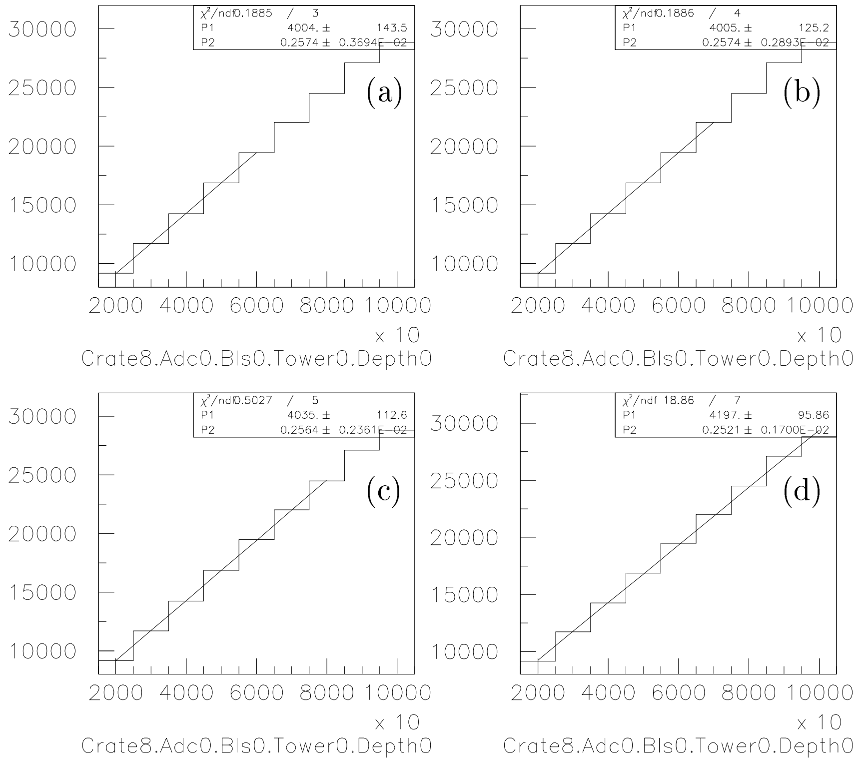

Figure 4.6: *Plots of the mean signal value as a function of the pulse amplitude with a fit on the: (a) first 5 points; (b) first 6 points; (c) first 7 points; (d) all points.*

value as shown in Fig. 4.9. This value was tested before the calibration system installation in the detector and was around 10 therefore the sigma value has to be checked another time with new runs as they seem to be related to other instabilities in the electronics chain. The ADC cards for which there are higher values of the sigmas are seen in the plots of the second parameter of the fit (cf. Fig. 4.10).

A surprising result is that crate 3, which has a strange result in mean studies, has a sigma value in agreement with the others. This result tells us probably that crate 3 has no bad channels problem but the observed behaviour is related to readout timing problem. Indeed in runs taken subsequently, the problem in crate 3 disappeared after readjustement of the readout timing.

The same studies on sigma from the curves of amplitude give the same results. The sigma value is varing from 0 to 100 while it was around 10 before the installation. This time, there is no relation between a high sigma and the values of the fit parameters. So all plots have to be checked. Nevertheless, the problems are generally at high value of amplitude which means close to the saturation.

The sigma values allow a second control of the electronics. With the set of runs used in these first studies, the values of the sigma does not corresponds to the value obtained

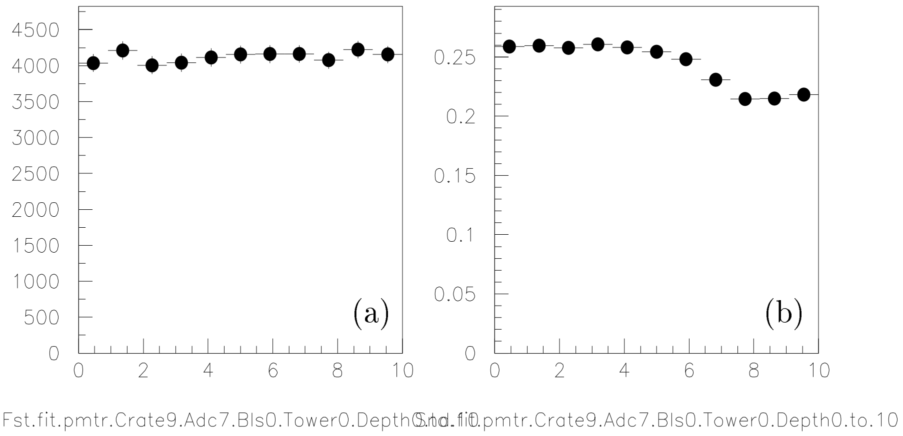

Figure 4.7: *(a) Pedestal as a function of channels; (b) slope value from the linear fit as a function of channels. One can observe a decrease on the slope value for hadronic channels which is not visible on pedestal plot.*

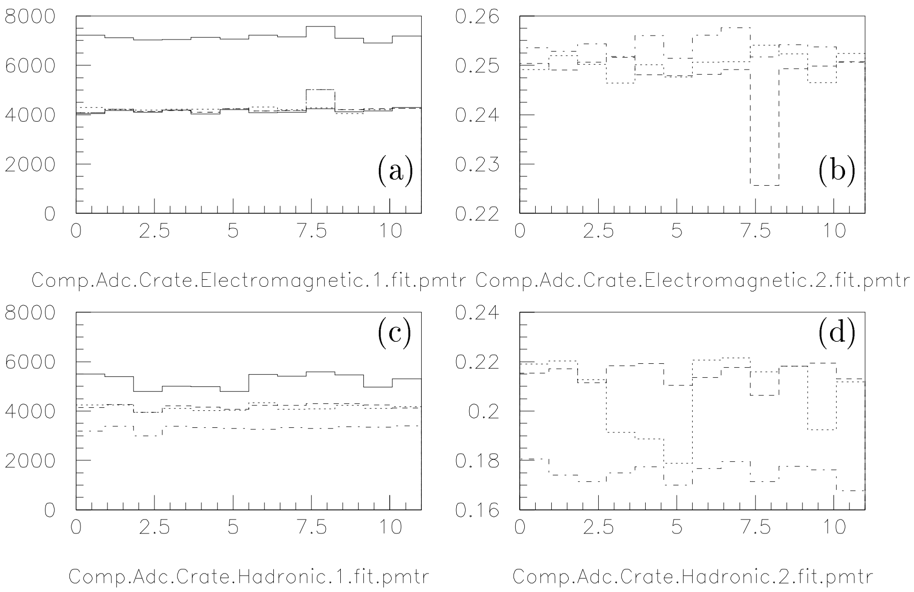

Figure 4.8: *Superimposition of the pedestal for the 4 crates of the central calorimeter for: (a) electromagnetic channels; (c) hadronic channels. Superimposition of the slope value for the 4 crates of the central calorimeter for: (b) electromagnetic channels; (d) hadronic channels.*

during the tests before installation in the detector. Moreover, these runs were not taken with optimal delay value so others studies still need to be done.

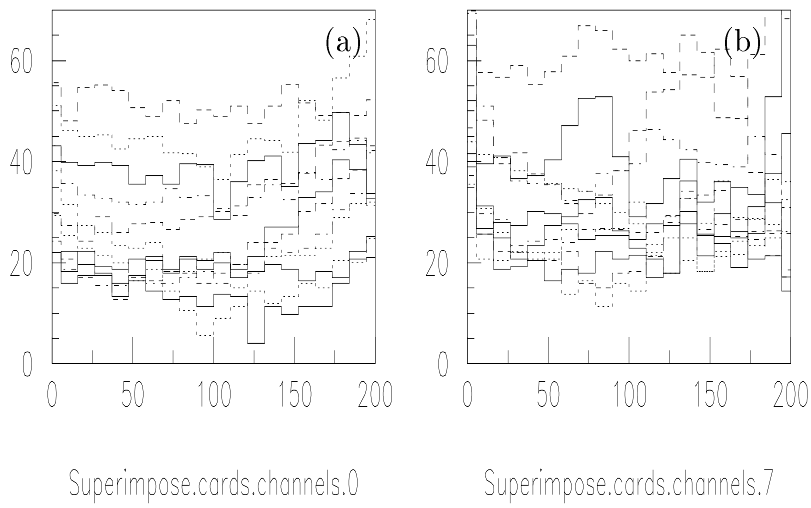

Figure 4.9: *Superimposition for all cards of crate 9 of the value of sigma for two different channels: (a) an electromagnetic channel; (b) a hadronic channel.*

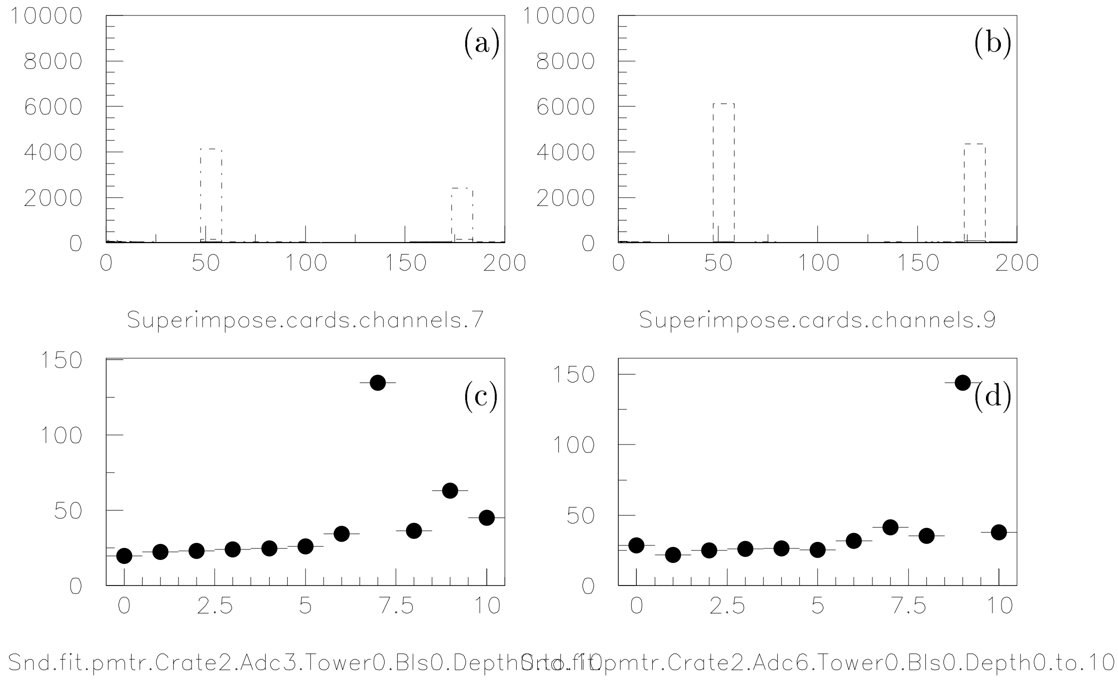

Figure 4.10: *On crate 2, (a) and (b) represent the cards with a bad sigma; (c) and (d) represents a strange second fit parameter value for this cards.*

Conclusion

These first calibration runs allowed to determine if some cards or crates were not working properly. More precise measurements and analyses need to be done especially for the amplitude parameters. For the delay we find an optimal value between 70 and 90 units of delay for all crates but for amplitude studies, we have not solved yet the disagreement in the pedestal value with the other results obtained at Fermilab. However we know already that these runs have been made with a value of delay of 50 which is a non optimal value. New runs have to be taken with another optimized delay value to have a more reliable value of the pedestal. The variation of the delay as a function of the channels (electromagnetic or hadronic channels) is important as we will have to choose a delay as a function of the capacitance of the detector cells or derive a correction function if we do not pulse at the optimum delay value.

The slopes obtained when varying the amplitude are stable so we have a good linearity and efficient uniformity. The value of the slope is needed to derive the energy from the readout signal. The pedestal value has to be subtracted to the signal in order to obtain the exact signal amplitude. So these two values influence directly the error made on the energy measurement and resolution. The linearity slope is determined in our study with a precision of 1.1%.

Bibliography

[1] DØ Collaboration, *Report of the Tevatron Higgs Working Group*, FERMILAB-Conf-00-279-T, M. Carena, J.S. Conway, H.E. Haber and J.D. Hobbs, hep-ph/0010338 (2000).

[2] S. Glashow, Nucl. Phys. **22** (1961) 569.
A. Salam, J. C. Ward, Phys. Rev. Lett. **13** (1964) 168.
S. Weinberg, Phys. Rev. Lett. **19** (1967) 1264.

[3] Y. Golfand and E. Likthman, JETP Lett. **13** (1971) 323.
D. Volkov and V. Akulov, Phys. Lett. B **46** (1973) 109.
J. Wess and B. Zumino, Nucl. Phys. B **70** (1974), Nucl. Phys. B **78** (1974) 1.

[4] LEP Higgs Working Group, *The standard model Higgs boson search at LEP: Result with the 2000 data; Request for LEP Running in 2001*, Submitted to the LEP Committee and to the CERN Research Board (2000).

[5] DØ Collaboration, *The DØ detector upgrade*, FERMILAB-Conf-95-030-E,
E. Borchi, S. Majewski, J. Huston, A. Penzo and P. G. Rancoita, Nucl. Phys. **B**, Proc. Suppl. 44 (1995) 12.

[6] DØ Collaboration, *DØ Silicon Tracker Technical Design Report*, DØ Note 2169, (1994).

[7] G. Alexeev *and al.*, *Technical Design Report of the DØ Forward Muon Tracking Detector Based on Mini-drift Tubes*, DØ Note 3366 (1997).

[8] DØ Collaboration, *Technical Design Report of the Calorimeter Electronics Upgrade for Run II* (1998).

[9] B. Olivier, *Recherche du partenaire supersymétrique du quark Top et contribution à l'amélioration de la calorimétrie de l'expérience DØ pour la phase II du Tevatron*, thèse de doctorat soutenue à l'Université Paris 6 (2001).

[10] DØ Collaboration,*The DØ Upgrade - Forward Preshower, Muon System, Level 2 Trigger, DØ Note 2894* (1996).